



**HAL**  
open science

# Effect of thermal annealing on the morphology of sol–gel processed barium strontium titanate thin films: Consequences on electrical properties

C. Mansour, M. Benwadih, G. Chahine, Christine Revenant

## ► To cite this version:

C. Mansour, M. Benwadih, G. Chahine, Christine Revenant. Effect of thermal annealing on the morphology of sol–gel processed barium strontium titanate thin films: Consequences on electrical properties. *AIP Advances*, 2020, 10 (6), pp.065204. 10.1063/5.0007242 . hal-02745929

**HAL Id: hal-02745929**

**<https://hal.science/hal-02745929>**

Submitted on 20 May 2022

**HAL** is a multi-disciplinary open access archive for the deposit and dissemination of scientific research documents, whether they are published or not. The documents may come from teaching and research institutions in France or abroad, or from public or private research centers.

L'archive ouverte pluridisciplinaire **HAL**, est destinée au dépôt et à la diffusion de documents scientifiques de niveau recherche, publiés ou non, émanant des établissements d'enseignement et de recherche français ou étrangers, des laboratoires publics ou privés.



Distributed under a Creative Commons Attribution 4.0 International License

# Effect of thermal annealing on the morphology of sol-gel processed barium strontium titanate thin films: Consequences on electrical properties

Cite as: AIP Advances 10, 065204 (2020); <https://doi.org/10.1063/5.0007242>

Submitted: 10 March 2020 • Accepted: 16 May 2020 • Published Online: 02 June 2020

 C. Mansour, M. Benwadih,  G. A. Chahine, et al.



View Online



Export Citation



CrossMark

## ARTICLES YOU MAY BE INTERESTED IN

[Ferroelectric thin films: Review of materials, properties, and applications](#)

Journal of Applied Physics **100**, 051606 (2006); <https://doi.org/10.1063/1.2336999>

[BaTiO<sub>3</sub>-based piezoelectrics: Fundamentals, current status, and perspectives](#)

Applied Physics Reviews **4**, 041305 (2017); <https://doi.org/10.1063/1.4990046>

[Sol-gel derived barium strontium titanate thin films using a highly diluted precursor solution](#)

AIP Advances **11**, 085302 (2021); <https://doi.org/10.1063/5.0055584>



# Effect of thermal annealing on the morphology of sol-gel processed barium strontium titanate thin films: Consequences on electrical properties

Cite as: AIP Advances 10, 065204 (2020); doi: 10.1063/5.0007242

Submitted: 10 March 2020 • Accepted: 16 May 2020 •

Published Online: 2 June 2020



View Online



Export Citation



CrossMark

C. Mansour,<sup>1</sup> M. Benwadih,<sup>1</sup> G. A. Chahine,<sup>2</sup> and C. Revenant<sup>3,a)</sup>

## AFFILIATIONS

<sup>1</sup>University Grenoble Alpes, CEA, LITEN, 38000 Grenoble, France

<sup>2</sup>University Grenoble Alpes, Grenoble-INP, SIMaP, 38000 Grenoble, France

<sup>3</sup>University Grenoble Alpes, CEA, IRIG-MEM, 38000 Grenoble, France

<sup>a)</sup>Author to whom correspondence should be addressed: [christine.revenant@cea.fr](mailto:christine.revenant@cea.fr). Tel.: +33 (0)4 38 78 97 81

## ABSTRACT

The link between the morphology and the electrical properties of the sol-gel processed  $\text{Ba}_{0.7}\text{Sr}_{0.3}\text{TiO}_3$  thin films is investigated. Previous studies have not fully explained the differences in growth morphology as a function of the elaboration conditions. The thin films were investigated by Grazing Incidence Small-Angle X-ray Scattering (GISAXS), x-ray diffraction, and scanning electron microscopy. More precisely, prototype films were studied as a function of the annealing temperature: at low temperatures (140 °C–200 °C) by *in situ* GISAXS and at high temperatures (600 °C–800 °C) by *ex situ* GISAXS. At ~150 °C, self-organized domains with a preferential distance of approximately 14 nm are formed. At high annealing temperatures, the growing domains become either nanoparticles or pores with a preferential distance of approximately 85 nm at 600 °C. This growth evolution is successfully explained by a general model based on convection and evaporation. With thermal annealing, the characteristic lengths parallel to the surface increase due to convection and the characteristic lengths perpendicular to the surface decrease due to evaporation. In addition, two types of annealing were investigated at 700 °C. For annealing after each other layer, a growth with vertically shifted particles occurs with no ferroelectric behavior. On the contrary, for annealing after each deposited layer, a columnar growth occurs and a ferroelectric hysteresis loop is obtained. The ferroelectricity of the sol-gel barium strontium titanate thin films is definitely linked to the complete removal of organic constituents leading to columnar growth.

© 2020 Author(s). All article content, except where otherwise noted, is licensed under a Creative Commons Attribution (CC BY) license (<http://creativecommons.org/licenses/by/4.0/>). <https://doi.org/10.1063/5.0007242>

## I. INTRODUCTION

Nowadays, tremendous research has been carried out on ferroelectric materials regarding their wide applications. Ferroelectric thin films are used for numerous micro-sensors and actuators.<sup>1</sup> Ferroelectric materials can be used as good pyroelectric candidates for infrared detectors or energy harvesting.<sup>2</sup> Among the lead-free pyroelectric materials, barium strontium titanate (BST) is intensively studied due to its high pyroelectric coefficient<sup>3</sup> and is also used for microwave applications.<sup>4</sup> The BST films are typically elaborated by sintering,<sup>5</sup> sputtering,<sup>6</sup> or sol-gel.<sup>7,8</sup> Sol-gel BST thin films may be

ferroelectric.<sup>9,10</sup> The advantages of the sol-gel elaboration are simplicity, the possibility of deposition on large surfaces, even flexibility, and low cost. Multiple sol-gel layers are usually deposited in order to reach the desired final film thickness. Between each sol-gel deposited layer, at least one thermal annealing is performed in order to remove a large amount of organic constituents. During annealing, nuclei occur and then form fractal aggregates, which are often studied with the Diffusion-Limited Aggregation (DLA) model.<sup>11</sup> For  $\text{Ba}_x\text{Sr}_{1-x}\text{TiO}_3$ , the annealing temperature necessary for crystallization and the Curie temperature increase with  $x$ .<sup>12,13</sup> Hence, a good compromise seems to be  $x \sim 0.7$ , in order to get a Curie temperature

slightly above room temperature without using very high annealing temperatures.

For many applications, the dielectric performances are crucial. As an example, for pyroelectric applications, the figure of merit is inversely proportional to the dielectric constant. Hence, at a constant pyroelectric coefficient, a low dielectric constant favors a high pyroelectric figure of merit. One simple possibility of decreasing the dielectric constant of BST layers is to introduce porosity, which intrinsically occurs during the sol–gel process. For  $\text{Ba}_{0.7}\text{Sr}_{0.3}\text{TiO}_3$  samples prepared by sol–gel with grain sizes less than  $1\ \mu\text{m}$ , permittivity decreases swiftly with decrease in the grain size.<sup>14</sup> Permittivity of  $\text{Ba}_{0.7}\text{Sr}_{0.3}\text{TiO}_3$  samples prepared by sol–gel has typical values from 200 to 400 with the annealing temperature varying from  $600\ ^\circ\text{C}$  to  $800\ ^\circ\text{C}$ .<sup>7</sup>

Moreover, previous studies of sol–gel  $\text{BaTiO}_3$  and  $\text{SrTiO}_3$  thin films have shown different morphologies according to the individual layer thickness.<sup>15</sup> For a thickness up to typically 10–20 nm, columnar growth occurs. Although sol–gel films are widely used, the underlying physical processes governing the film evolution from the liquid state up to the dry one are not yet clearly understood, and a general model describing the thin film formation would be of the utmost importance. The novelty of the present research lies in unraveling the drastic morphology evolution from the liquid film up to the dry one as a function of thermal annealing up to  $800\ ^\circ\text{C}$ . Grazing Incidence Small-Angle X-ray Scattering (GISAXS) is, indeed, a powerful technique to probe sol–gel thin films,<sup>16,17</sup> leading to a better knowledge of such films.<sup>18</sup> As a matter of fact, x rays are particularly well-adapted for liquid or gel films for which microscopy studies are difficult, x rays yield statistical information, and *in situ* x-ray experiments can be carried out as a function of thermal annealing. More precisely, the GISAXS technique allows us to obtain characteristic sizes in the directions parallel and perpendicular to the surface. First, the GISAXS technique was used extensively to study the film morphology from the very beginning of organic–inorganic phase separation (with *in situ* measurements) up to the formation of particles and pores (with *ex situ* measurements) as a function of the annealing temperature. The effects of the annealing time from 5 min to 60 min and of the substrate ( $\text{SiO}_2$  or Pt) were also investigated. Annealing at high temperatures after each layer deposit or each other layer deposit was also studied. Based on the *in situ* GISAXS observations, at the very beginning of the liquid film annealing, we develop a general model for sol–gel film formation based on the physics of fluids at the nanoscale.<sup>19</sup> Finally, optimized annealing conditions allow us to obtain ferroelectric sol–gel BST thin films.

## II. EXPERIMENTAL DETAILS

A BST commercial solution from Mitsubishi Materials Corporation was used. It comprised of 7 wt. % of  $(\text{Ba}_{0.7}\text{Sr}_{0.3})\text{TiO}_3$  precursors, 88 wt. % of isoamyl acetate, and 5 wt. % of isoamyl alcohol. Thermogravimetric analysis (TGA) was used to determine the thermal decomposition properties of the dried BST solution. The sol–gel solution was dried at  $150\ ^\circ\text{C}$  for 24 h in air prior to the TGA analysis. The TGA study was conducted by heating the dried gel in air from  $30\ ^\circ\text{C}$  to  $800\ ^\circ\text{C}$ .

For the fundamental study, the solution was deposited on the  $\text{SiO}_2$  ( $3\ \mu\text{m}$ )/Si ( $725\ \mu\text{m}$ ) or Pt ( $200\ \text{nm}$ )/Cr ( $20\ \text{nm}$ )/ $\text{SiO}_2$  ( $3\ \mu\text{m}$ )/Si ( $725\ \mu\text{m}$ ) substrates by spin-coating. As a matter of fact, Pt is used as

a capacitor electrode. The substrates were cleaned with acetone and isopropanol in an ultrasonic cleaner and then rinsed with deionized water. The BST films were spun at 300 rpm for 10 s, then, 1000 rpm for 30 s on the substrate. The as-deposited films were pre-annealed on a hot plate at  $130\ ^\circ\text{C}$  for 5 min for pyrolysis and  $360\ ^\circ\text{C}$  for 5 min for organic decomposition, similar to the annealing process used for BST capacitors.<sup>20</sup> For the five deposited layers, the deposition-pre-annealing cycle was repeated five times before the final annealing. The samples were annealed at  $600\ ^\circ\text{C}$  for 1 h and a half on a hot plate, and at  $700\ ^\circ\text{C}$  and  $800\ ^\circ\text{C}$  for 1 h in a conventional furnace under ambient air conditions. The thin films were observed by cross-sectional scanning electron microscopy (SEM), and the five layers were approximately 640 nm thick. For the capacitor study, the samples were spin coated on Pt/ $\text{TiO}_2$ / $\text{SiO}_2$ /Si at 4000 rpm for 30 s and baked at  $450\ ^\circ\text{C}$  for 5 min on a hot plate after each layer deposit. The samples were then annealed at  $700\ ^\circ\text{C}$  for 1 min in a furnace under ambient air atmosphere after either one or two deposited layers, corresponding to the 1 L or 2 L sample, respectively. The thickness of the film was approximately 440 nm.

The crystalline orientation of the BST thin films deposited on Pt was characterized by x-ray diffraction (XRD) on a Panalytical Empyrean diffractometer equipped with a Cobalt anode tube ( $\text{Co}\ \lambda\text{K}\alpha = 1.789\ \text{\AA}$ ) with a fixed  $1/4^\circ$  divergence slit, a Soller slit, a 4 mm mask as incident optics, and a parallel long plate collimator and a proportional one-dimensional detector as diffracted optics. The GISAXS experiment was performed at the European Synchrotron Radiation Facility (ESRF) on the BM02 beamline with an x-ray energy of 16 025 eV and an incident angle of  $0.16^\circ$ .<sup>21</sup> The critical angle was  $0.111^\circ$  for Si,  $0.297^\circ$  for Pt, and  $0.152^\circ$  for BST at  $600\ ^\circ\text{C}$  corresponding to a density of  $4.98\ \text{g cm}^{-3}$  (see Sec. III B). The attenuation length is the depth into the material measured along the surface normal where the x-ray intensity falls to  $1/e$  ( $\sim 0.37$ ) of its value at the surface. Then, the attenuation length was 62 nm, i.e., the morphology (such as pores) of the top deposited layer was probed. For the *in situ* GISAXS experiment, the solution was deposited on the  $\text{SiO}_2$ /Si substrate, annealed at  $130\ ^\circ\text{C}$  during 5 min prior to the experiment and a hot stage (Anton Paar DHS 900) was used in the ambient environment without the dome for *in situ* annealing up to  $200\ ^\circ\text{C}$ . The deposited solution was mainly formed of the isoamyl acetate liquid  $\text{C}_7\text{H}_{14}\text{O}_2$  with a density of  $0.876\ \text{g cm}^{-3}$ , corresponding to a critical angle of  $\sim 0.07^\circ$ . For isoamyl acetate, the attenuation length was as large as  $26\ \mu\text{m}$ , i.e., the morphology of the deposited solution was probed through the whole film thickness. The GISAXS analysis was performed with the FitGISAXS software.<sup>22</sup>

For the electrical measurements, electrodes of 200 nm thick Pt were deposited by evaporation onto the samples through a shadow mask to form BST thin film capacitors. The capacitance and dissipation factors in the range of 20 Hz–1 MHz were measured using the Agilent E4980A Precision LCR Meter. Hysteresis loops were measured using a Precision 10 kV HVI-SC from Radiante Technologies.

## III. RESULTS AND DISCUSSION

### A. One deposited layer

In order to address the loss evolution of the organic constituents, TGA measurement was performed from room

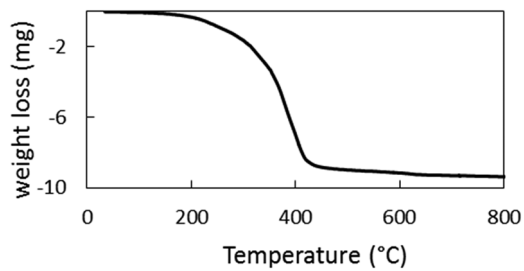


FIG. 1. TGA curve from RT to 800 °C.

temperature (RT) to 800 °C (Fig. 1). This curve indicates that the weight of the BST solution begins to decrease at approximately 140 °C, corresponding to the boiling temperature of isoamyl acetate (142 °C). A sharp decrease in the weight occurs from 200 °C to

400 °C corresponding to the removal of the organic compounds. Above 440 °C, the weight loss is very small indicating that most of the organic compounds have evaporated.

In order to gain insight into the statistical morphology of the films, GISAXS measurements were performed as a function of  $q_y$ , the momentum transfer parallel to the sample surface and,  $q_z$ , the momentum transfer perpendicular to the sample surface. Figure 2 displays *in situ* GISAXS images of one liquid BST layer on SiO<sub>2</sub>/Si at 25 °C, and successively annealed at 137 °C, 150 °C, 190 °C, and 200 °C for 5 min at each temperature. Between each annealing, the GISAXS measurement was performed at RT. In addition, horizontal cuts were performed as a function of  $q_y$  at the critical angle, as well as vertical cuts as a function of  $q_z$  (Fig. 3). The initial state has a scattering at high  $q_z$ , indicating an electronic density contrast. More precisely, the scattering peak has a  $q_z$  maximum at  $\sim 1.73 \text{ nm}^{-1}$ . The thickness is determined by  $\Delta q_z$  between two nearby  $q_z$  minima. Here,  $\Delta q_z \sim 0.9 \text{ nm}^{-1}$  corresponds to a layer thickness of

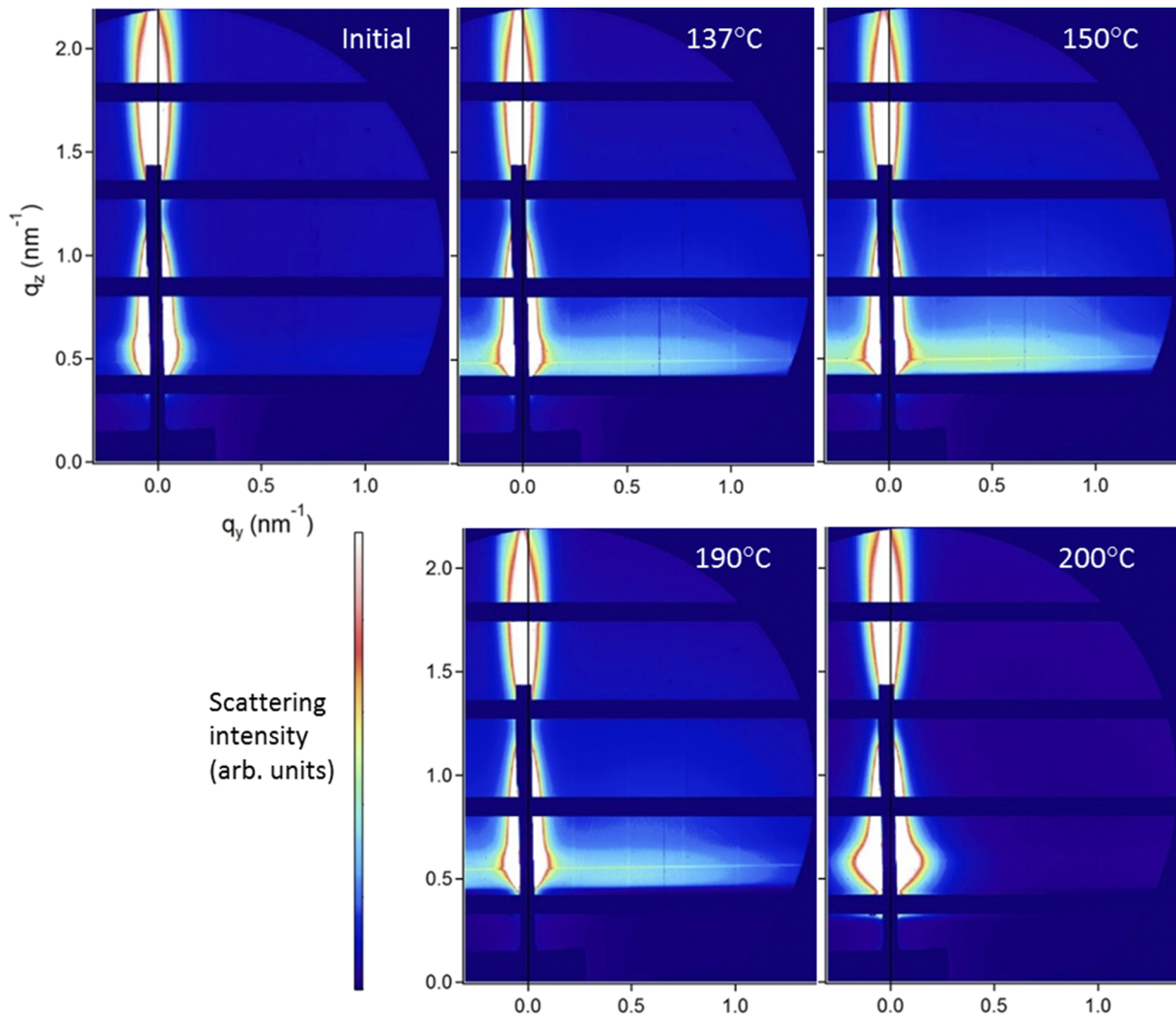
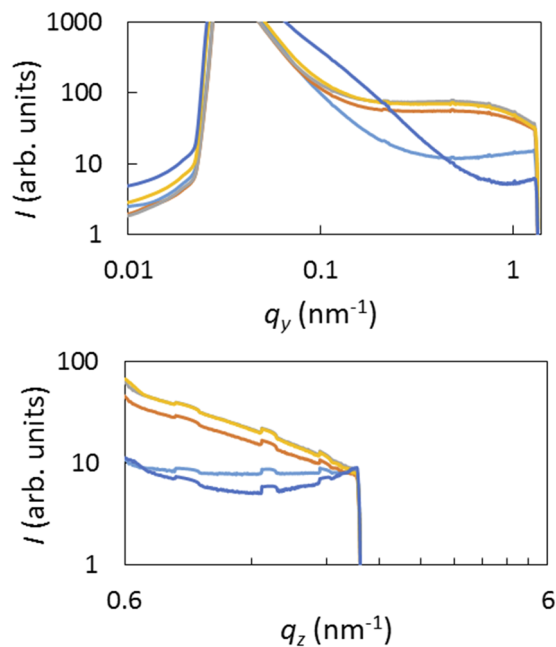


FIG. 2. *In situ* GISAXS images of one liquid BST layer on SiO<sub>2</sub>/Si at 25 °C and successively annealed at 137 °C, 150 °C, 190 °C, and 200 °C.



**FIG. 3.** Linescans as a function of  $q_y$  at the critical angle and as a function of  $q_z$  with logarithmic scales: initial state (light blue), annealing at 137 °C (orange), at 150 °C (gray), at 190 °C (yellow), and at 200 °C (dark blue). The “bumps” originate from the dark regions in the detector and are, of course, not taken into account for the slope calculation.

approximately 7 nm. This means that the inorganic compounds are not homogeneously distributed in the solvent-rich film. In order to explain the 7-nm layer at the surface of the initial BST film, let us compare the surface tension of the different compounds. No value of the BST surface tension was found in the literature. Nevertheless, the surface tension of  $\text{BaTiO}_3$  is approximately 2.6 N/m for the bulk and 0.68 N/m for nanowires<sup>23</sup> and that of isoamyl acetate is 24 mN/m.<sup>24</sup> As the surface tension of the inorganic compound is larger than that of the solvent, there is a depletion layer (poor in BST) of thickness  $\xi$  near the free surface. Such an effect has already been put as evidence in other systems.<sup>25</sup> The parameter  $\xi$  corresponds to the characteristic size of the inorganic compound.

Moreover, Fig. 2 shows that there is a slight scattering at high  $q_y$  ( $\sim 1 \text{ nm}^{-1}$ ) coming from tiny particles distributed in the entire solvent. After an annealing at 137 °C, above the boiling temperature of isoamyl alcohol (132 °C), a wide (respectively, thin) scattering appears along  $q_y$  (respectively,  $q_z$ ), indicating narrow columnar domains. Between adjacent domains, the solvent/inorganic fraction changes. A solvent-rich (inorganic-poor) domain is adjacent to a solvent-poor (inorganic-rich) domain. After annealing at 150 °C, the wide scattering has maximum visibility in Fig. 3 at  $q_y \sim 0.46 \text{ nm}^{-1}$ , corresponding to a preferential distance parallel to the surface  $D \sim 14 \text{ nm}$  between two similar columnar domains (with similar electronic densities, i.e., organic-rich or inorganic-rich domains).

After annealing at 190 °C, the scattering has a smaller extension along  $q_y$ , meaning that the domains grow. At high  $q_y$  or  $q_z$ , the curves  $\ln(I)$  may vary linearly as a function of  $\ln(q_y)$  or  $\ln(q_z)$ , indicating

that the intensity varies as  $q^{-n}$ , where the exponent  $n$  is characteristic of the sharpness of the diffusing entity.<sup>26</sup> For  $q_y$  and  $q_z$  larger than  $1 \text{ nm}^{-1}$ , the slope of  $\ln(I)$  is found to be similar for  $\ln(q_y)$  and  $\ln(q_z)$  and is approximately  $-1.4$  for annealing at 137 °C,  $-1.6$  at 150 °C, and  $-1.7$  at 190 °C (Fig. 3). These exponents do not correspond to a simple geometrical shape. For example,  $n = 2$  in the direction perpendicular to a plane,  $n = 3$  in the direction perpendicular to the curved surface of a cylinder, and  $n = 4$  for a sphere. Hence, the exponents correspond to the fractal dimension of the particles.<sup>27</sup> Fractals exhibit similar patterns at increasingly small scales, i.e., the scattering domains have a “zigzag” interface. The experimental exponents are in the range of that found for DLA in 2D models (1.67).<sup>11</sup> Finally, after an annealing at 200 °C, the scattering shrinks along  $q_y$ , revealing larger domains. This *in situ* GISAXS experiment brings general knowledge about the very beginning of the sol-gel thin film formation starting from the liquid film. A density modulation occurs parallel to the surface indicating that a rich-organic domain is next to a rich-inorganic domain. In order to get an inorganic crystallized BST thin film, the annealing temperature was increased in order to go on with the evaporation of the organic constituents and to crystallize the BST film.

A kinetic study was also performed at 600 °C in order to follow the morphology evolution as a function of the annealing time. Figure 4 displays *ex situ* GISAXS images of one deposited BST layer on  $\text{SiO}_2/\text{Si}$  annealed at 600 °C during different times from 5 min to 60 min. The scattering shape is quite similar for an annealing time from 5 min to 30 min. On the contrary, after an annealing of 60 min, the scattering shrinks along  $q_y$  indicating that the pores are wider in the direction parallel to the surface. In addition, there is an interference peak at  $q_y \sim 0.074 \text{ nm}^{-1}$ , corresponding to a preferential distance  $D$  between the pores of  $\sim 85 \text{ nm}$ , larger than that obtained at a low annealing temperature ( $\sim 150$  °C). Hence, the preferential distance increases with the annealing temperature. Moreover, the angle of total external reflection (Yoneda peak) is smaller for 60 min than for lower annealing times indicating that the film is less dense, i.e., more porous. This kinetic study puts in evidence the long annealing time necessary to remove the organic constituents in one thick deposited layer.

Hence, at low annealing temperatures, a density modulation occurs between adjacent domains in the liquid film. A phase separation between organic-rich and inorganic-rich domains occurs. Upon annealing at higher temperatures, the organic-rich domains become pores due to the evaporation of the organic constituents and the inorganic-rich domains become particles.

## B. Several deposited layers

Several BST layers were deposited and annealed at 600 °C, 700 °C, or 800 °C. Figure 5 displays the GISAXS images of such BST thin films. The scattering from the pores is globally similar to that obtained for one deposited layer, indicating that the pores have globally the same shape and size. This means that the pores are delimited below/above by particles, i.e., there is no columnar growth. Moreover, the effect of the substrate was studied by probing the BST thin films deposited either on  $\text{SiO}_2/\text{Si}$  or on  $\text{Pt/Cr}/\text{SiO}_2/\text{Si}$  used for technological applications.

For deposit on  $\text{SiO}_2/\text{Si}$ , from 600 °C to 800 °C, the scattering is relatively similar, meaning that the pores have a similar size. The

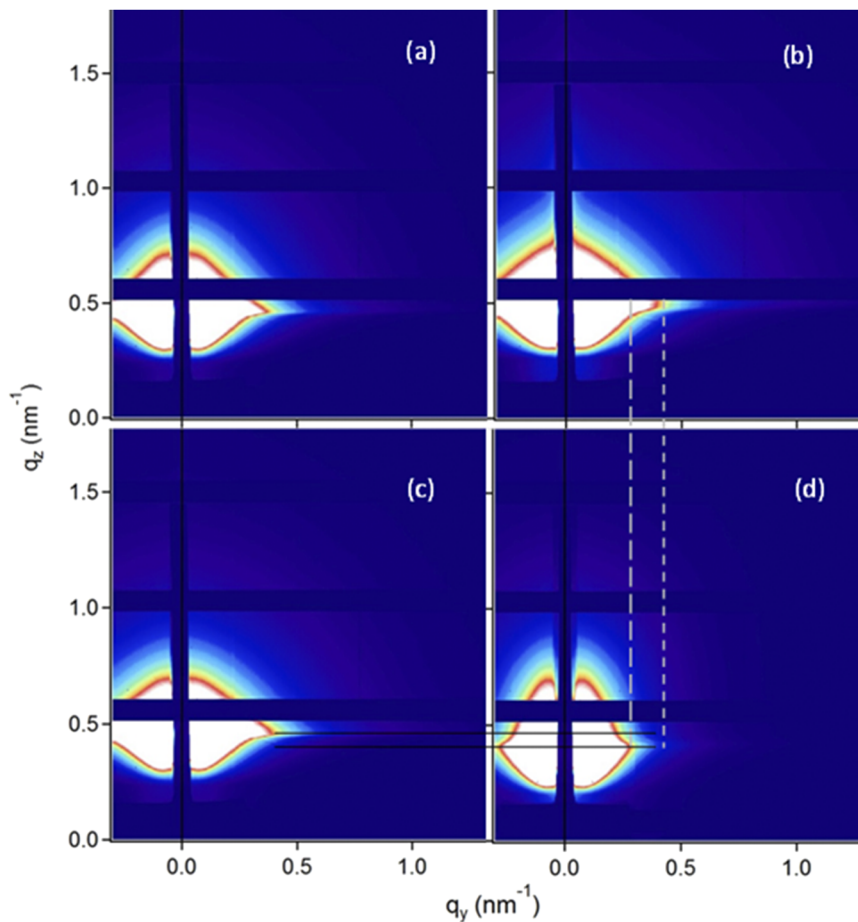


**FIG. 4.** *Ex situ* GISAXS images of one deposited BST layer annealed at 600 °C during (a) 5 min, (b) 15 min, (c) 30 min, or (d) 60 min. The horizontal black lines indicate the intensity maximum (Yoneda peak) for 30 min and 60 min. Vertical lines are positioned at the yellow limit of the peak for 15 min (small dash) and 60 min (large dash).

scattering extension along  $q_z$  is larger than that along positive  $q_y$ , indicating that the pores have an oblate spheroid shape. For deposit on Pt, the pores have also an oblate spheroid shape. Moreover, as the annealing temperature increases, the scattering extends slightly further along  $q_z$ , indicating that the height of the pores slightly decreases, and the scattering extends further along  $q_y$ , indicating that the radius of the pores decreases. The scattering extends further compared to that for the SiO<sub>2</sub>/Si deposit, indicating that the pores are smaller compared to those for the SiO<sub>2</sub>/Si deposit.

Interestingly, GISAXS can be used to estimate the film porosity. In GISAXS, the intensity maximum (Yoneda peak) as a function of the out-of-plane angle occurs at the critical angle  $\alpha_c$  for total external reflection. As a matter of fact, the material density  $\rho$  can be expressed as

$$\rho = \frac{\pi \alpha_c^2 \bar{M}}{r_e N_A (Z + f') \lambda^2}, \quad (1)$$

where  $M$  is the molecular weight,  $r_e$  is the classical electron radius,  $N_A$  is the Avogadro's number,  $Z$  is the number of electrons per atom,  $f'$  is the dispersion correction, and  $\lambda$  is the x-ray wavelength. The average molecular weight of Ba<sub>0.7</sub>Sr<sub>0.3</sub>TiO<sub>3</sub> is obtained from the sum

of the relative atomic masses of each constituent element. The dispersion correction  $f'$  for a given element can be obtained from the x-ray interaction database.<sup>28</sup> The porosity  $\phi$  of the film is

$$\phi = 1 - (\rho/\rho_0), \quad (2)$$

where  $\rho_0$  is the bulk mass density of the Ba<sub>0.7</sub>Sr<sub>0.3</sub>TiO<sub>3</sub>. This bulk mass density is obtained from that of BaTiO<sub>3</sub> (6.02 g cm<sup>-3</sup>) and that of SrTiO<sub>3</sub> (5.11 g cm<sup>-3</sup>). Hence,  $\rho_0 \sim 5.747$  g cm<sup>-3</sup> for bulk Ba<sub>0.7</sub>Sr<sub>0.3</sub>TiO<sub>3</sub>.

The GISAXS results for the five BST layers deposited on Pt are gathered in Table I. As the annealing temperature increases, the Yoneda peak shifts toward slightly larger angles  $\alpha_c$ , indicating that  $\rho$  also increases, and, hence,  $\phi$  decreases as shown in Table I. As the annealing temperature increases, the pore semi-axes (Table I) decrease, which is in agreement with the decrease in  $\phi$ . The pores have an oblate spheroid shape with an aspect ratio  $[(h/2)/r]$  approximately equal to 0.5. More precisely, the aspect ratio slightly increases as the annealing temperature increases.

The linear thermal expansion coefficient of Ba<sub>0.7</sub>Sr<sub>0.3</sub>TiO<sub>3</sub> is  $10.5 \times 10^{-6} \text{ }^\circ\text{C}^{-1}$ ,<sup>29</sup> that of Pt is  $9 \times 10^{-6} \text{ }^\circ\text{C}^{-1}$ ,<sup>30</sup> and that of Si is  $2.5 \times 10^{-6} \text{ }^\circ\text{C}^{-1}$ .<sup>30</sup> The thermal expansion coefficient of BST is larger than that of Pt and that of Si. During cooling, the substrate limits the

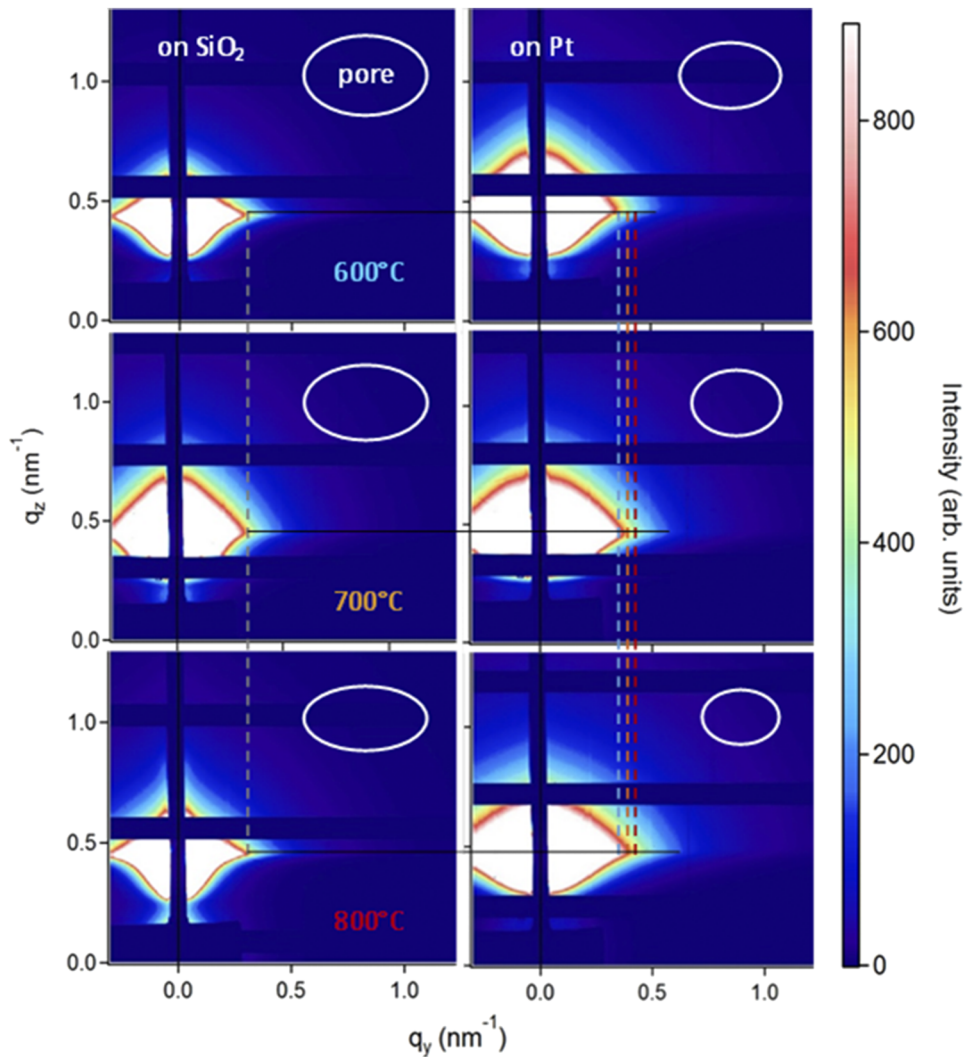


**FIG. 5.** GISAXS images of five deposited BST layers deposited on SiO<sub>2</sub>/Si (left column) or on Pt (right column) and annealed at 600 °C, 700 °C, and 800 °C. The horizontal black lines indicate the intensity maximum (Yoneda peak). The white ellipses represent schematically the pores. For SiO<sub>2</sub>/Si, the gray dashed line is positioned at the yellow limit of the peaks. For deposit on Pt, the vertical dashed lines are positioned at the yellow limit of the peak at 600 °C (blue), 700 °C (orange), and 800 °C (red).

BST layer contraction leading to a tensile stress for the BST layer. This stress can be at least partially relaxed by the pores, which adopt an oblate spheroid shape.

In addition, Fig. 6 displays the  $\theta$ - $2\theta$  XRD spectrum of BST films annealed at 600 °C, 700 °C, and 800 °C. The most intense peak

**TABLE I.** Critical angle  $\alpha_c$ , material density  $\rho$ , porosity  $\phi$ , semi-axes of the pores, namely, radius and half of the height, aspect ratio of the pores for the BST layers deposited on Pt and annealed at 600 °C, 700 °C, and 800 °C.

T (°C)	$\alpha_c$ (deg)	$\rho$ [g cm <sup>-3</sup> ]	$\phi$	r (nm)	h/2 (nm)	Aspect ratio
600	0.152	4.98	0.13	10	4.5	0.45
700	0.156	5.24	0.09	8.5	4	0.47
800	0.158	5.38	0.06	7	3.6	0.51

corresponds to the (111) peak of Pt. This peak has a broad basis corresponding to small Pt crystallites. The other peaks are the (100), (110), (200), (210), and (211) peaks of BST. The BST films are crystallized in one phase, namely, the perovskite structure. There is no preferential orientation indicating that the films are polycrystalline. The peaks of the BST films annealed at different temperatures are similar, indicating that the crystallinity does not significantly evolve above 600 °C. The cell parameters deduced from the XRD measurements are  $a = 3.95$  Å and  $c = 3.99$  Å, which are, respectively, slightly below and above the bulk parameter 3.974 Å (04-009-3218 of the ICDD PDF-4 database).<sup>7</sup> The  $\theta$ - $2\theta$  XRD spectrum probes the perpendicular direction to the surface. For the (100), (110), (200), and (210) peaks, the lattice vector  $c$  is aligned parallel to the surface corresponding to a flattened tetragonal structure. The tensile stress of the BST layers is also partially relaxed by the deformation of the grain structure. Moreover, the grain size deduced by the Scherrer formula corresponds to the grain size perpendicular to the surface.

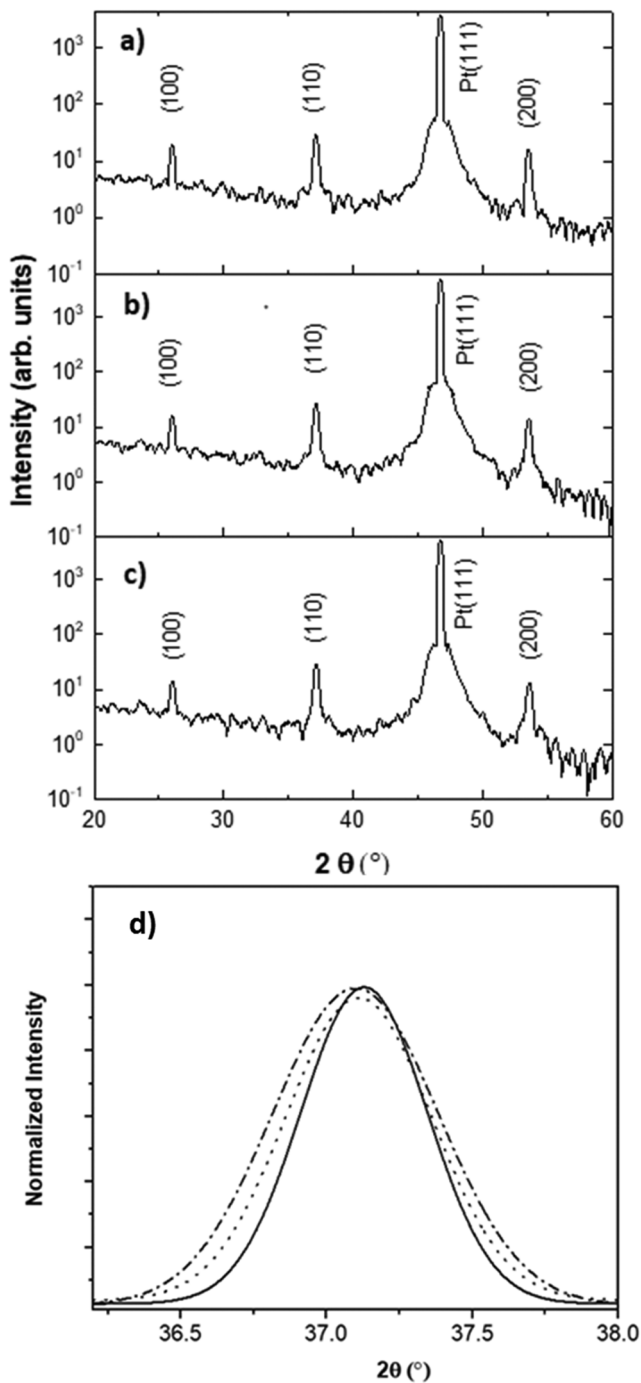


**FIG. 6.** XRD pattern of sol-gel BST thin films annealed at: (a) 600 °C, (b) 700 °C, and (c) 800 °C. (d) (110) XRD peak at 600 °C (full line), 700 °C (dashed line), and 800 °C (dotted line).

The full width at half maximum (FWHM) of the (110) peak yields  $\sim 17$  nm for the smaller crystallized grain size perpendicular to the surface, i.e., the grain height. More precisely, the diffraction peaks slightly broaden as the temperature increases, indicating that the

grain height slightly decreases as the temperature increases. This is coherent with the flattened tetragonal structure of the grains. For comparison, the grain height is larger than that of the pores. A height decrease was also observed for the pores as the temperature increases.

Furthermore, Fig. 7 shows the cross-sectional SEM images of BST films annealed at 600 °C, 700 °C, and 800 °C. A high density of nanoparticles (NPs) is visible, and the pores are delimited by particles in both directions parallel and perpendicular to the surface, i.e., there is no columnar growth.

Owing to the long annealing time necessary to remove organic constituents on a thick layer, high temperature annealing is now performed after the deposit of 1 L or 2 L, as shown in Fig. 8(a). Figure 8 (b) shows the cross-sectional SEM images of BST films deposited on Pt and annealed at 700 °C for 1 L or 2 L. The two annealing types correspond to two different morphologies. The 1 L annealing leads to a columnar growth, whereas the 2 L annealing leads to a granular growth.

Figure 9 displays the  $\theta$ - $2\theta$  XRD spectrum of the BST films after 1 L or 2 L annealing. The XRD peaks of BST previously observed in Fig. 6 are also present after 1 L or 2 L annealing. In Fig. 9, the shoulder on the Pt(111) peak at the low angle side corresponds to BST (111). The XRD spectra obtained after the two annealing types are similar, whereas the growth morphology is different. This means that the XRD comes from grains with a similar size, whatever the 1 L or 2 L annealing. Hence, for 1 L annealing, the BST columns are made of several stacked crystalline grains. These grains are similar to those which are vertically shifted in the granular growth after 2 L annealing. The 1 L or 2 L annealing determines the growth morphology, but the crystalline structure of the grains is similar.

### C. Convection model

The morphology of the sol-gel BST thin films is explained by a convection model described here. As the *in situ* GISAXS experiment performed at the very beginning of the film formation puts in evidence for columnar domains with different solvent fractions, let us consider the volume fraction of the solvent  $\psi$  from  $\psi_A$  (at point A) to  $\psi_B$  (at point B) in Fig. 10. Points A and B are in two different solvent fraction regions. Moreover, during evaporation, the volume fraction of the solvent decreases from  $\psi_d$  (down) at the bottom interface to  $\psi_u$  (up) at the free surface. The solution diffuses from a region with a larger solvent fraction toward a region with a smaller solvent fraction. The diffusion current in the film is

$$W = D_{coop}(\psi_d - \psi_u)/(a^3 \ell), \quad (3)$$

where  $D_{coop}$  is the cooperative diffusion of the solution,  $a$  is the size of a solvent molecule, and  $\ell$  is the film thickness.

An instability roll of lateral size  $e$  carries solvent from bottom to top (solvent fraction domain near A), from A to B, and from top to bottom (solvent fraction domain near B). The solvent fraction is slightly larger in domain A than in domain B. Domain B corresponds to a particle nucleation site.

Combined diffusion and convection lead to

$$D_{coop} \frac{\psi_A - \psi_B}{e} \cong V(\psi_d - \psi_u), \quad (4)$$

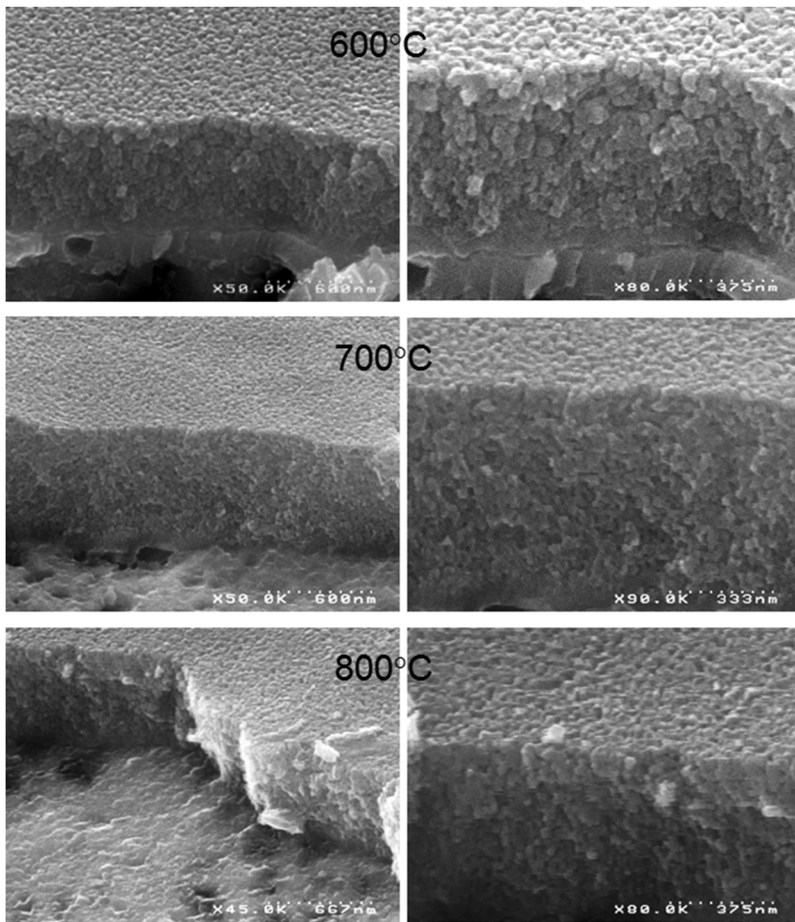


**FIG. 7.** Cross-sectional SEM images from the BST layers on Pt at different annealing temperatures: 600 °C (first row), 700 °C (second row), and 800 °C (third row). Left column: global view, and right column: more detailed view.

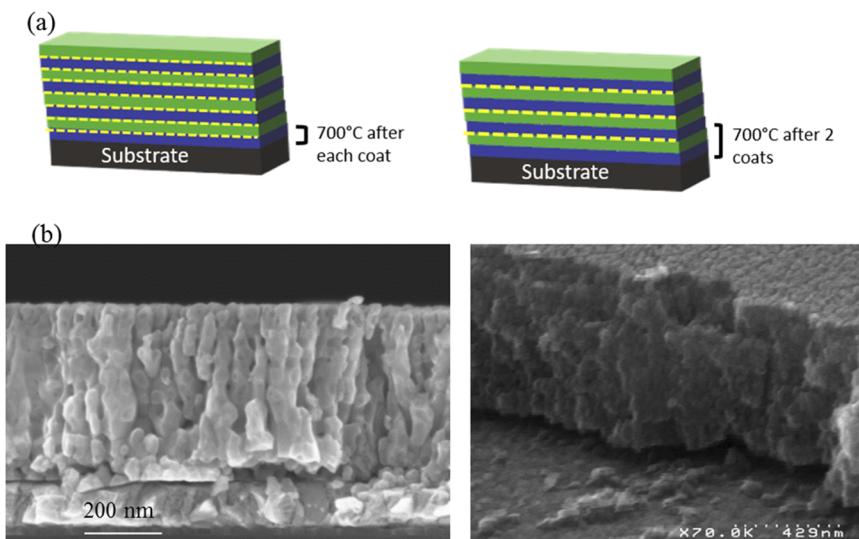


**FIG. 8.** High temperature annealing for 1 L (left) or 2 L (right). (a) Schematic of the sequence of deposition and annealing. The annealing is indicated by the yellow dashes. (b) SEM images of the corresponding BST films deposited on Pt and annealed at 700 °C.

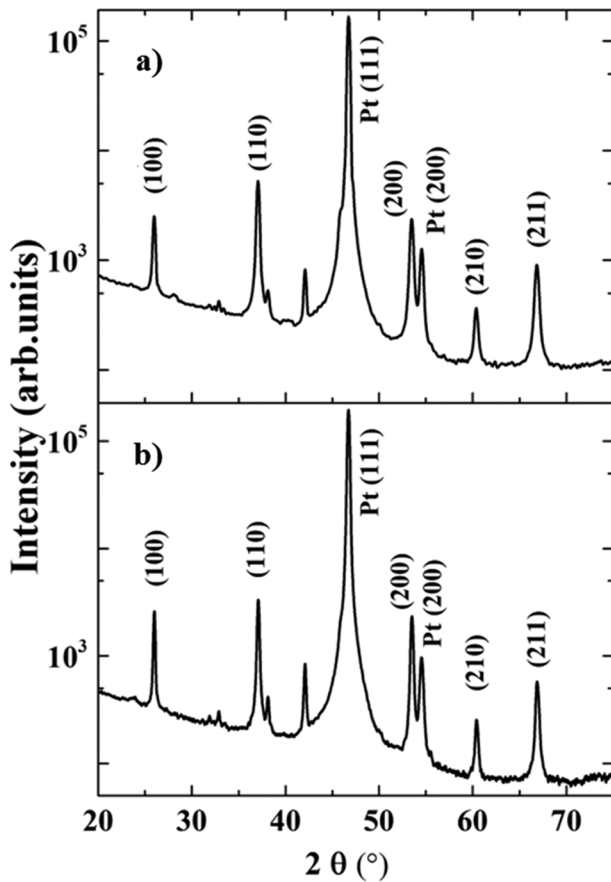


**FIG. 9.** XRD spectra of BST thin films deposited on Pt and annealed at 700 °C for (a) 1 L or (b) 2 L.

where  $V$  is the roll velocity. This parameter is estimated by a balance between the surface forces and viscous stresses,

$$\frac{\gamma_B - \gamma_A}{e} \sim \frac{\eta V}{e}, \quad (5)$$

where  $\gamma$  is the surface tension and  $\eta$  is the solution viscosity. The difference in the surface tension between point A and point B can be expressed as

$$\gamma_B - \gamma_A = |\gamma'|(\psi_A - \psi_B), \quad (6)$$

where  $\gamma' = d\gamma/d\psi$ .

Hence, the roll velocity becomes

$$V \sim \frac{|\gamma'|}{\eta} (\psi_A - \psi_B). \quad (7)$$

Moreover,  $D_{\text{coop}}$  is proportional to the thermal energy  $kT$  and inversely proportional to the solvent viscosity  $\eta_s$ , as well as the typical size  $\xi$  in the solution,

$$D_{\text{coop}} = \frac{kT}{\eta_s \xi}. \quad (8)$$

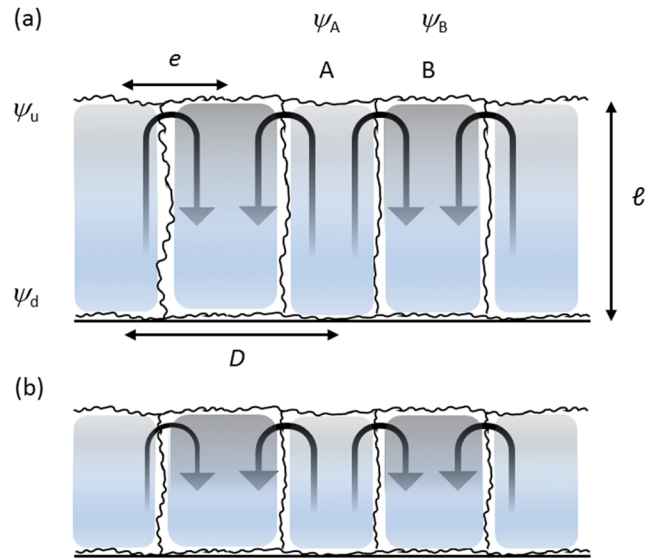


**FIG. 10.** Loops, represented by the black arrows, occur in the thin film due to evaporation and convection at low annealing temperatures. The inorganic fraction (respectively, solvent) is represented by gray (respectively, blue) shading. The inorganic fraction increases slightly from bottom to top as well as from domain A to domain B. (a) Beginning of the convective process, (b) advanced process of evaporation and convection. The layer thickness decreases due to evaporation.

Finally, the roll size  $e$  is

$$e \cong \frac{kT}{|\gamma'| \xi \eta_s (\psi_d - \psi_u)}. \quad (9)$$

At the beginning of annealing, the solution viscosity  $\eta$  is roughly that of the solvent  $\eta_s$  and the roll size becomes

$$e \cong \frac{kT}{|\gamma'| \xi (\psi_d - \psi_u)}. \quad (10)$$

The roll size increases with  $T$ , in agreement with the observed growth of domains at 150 °C, 190 °C, and 600 °C by GISAXS. The characteristic size  $\xi$  is 7 nm from the GISAXS measurements, and the parameter  $|\gamma'|$  is found to be equal to 0.66 N/m by using the values of the surface tension of nano-sized BaTiO<sub>3</sub> and of isoamyl acetate. The roll size  $e$  is also equal to the size of a domain with a similar solvent fraction and is approximately half the periodic distance  $D$ . Hence, the domain size and the periodic distance increase with  $T$ . After an annealing at 150 °C, the observed roll size  $e$  of ~7 nm corresponds to an extremely small difference between the solvent fraction at the bottom interface and at the free surface  $\psi_d - \psi_u \sim 0.02\%$ . Note that this beginning in phase separation between the solvent/inorganic constituents is prior to any crystallization.

Furthermore, due to the solvent evaporation, the film thickness decreases as follows:

$$d\ell/dt = -a^3 W. \quad (11)$$

Combining (3) and (11), one gets

$$D_{\text{coop}} = \frac{\ell(d\ell/dt)}{\psi_d - \psi_u}. \quad (12)$$

Combining (8) and (12), the time  $\Delta t$  corresponding to the decrease in the film thickness  $\Delta \ell$  is

$$\Delta t = \frac{\eta_s \xi}{kT} \frac{\ell \Delta \ell}{\psi_d - \psi_u}. \quad (13)$$

Let us note that  $\ell_i$  (respectively,  $\ell_d$ ) is the thickness of the initial (respectively, dry) film. Finally, by using  $\ell = \ell_i$ ,  $\Delta \ell = \ell_i - \ell_d$ , and  $\ell_d = \ell_i \times x_{si}$  with  $x_{si}$  the initial solid fraction,  $\Delta t$  becomes

$$\Delta t = \frac{\eta_s \xi}{kT} \frac{\ell_i^2 (1 - x_{si})}{\psi_d - \psi_u}. \quad (14)$$

The evaporation time is inversely proportional to the temperature and to the difference between the solvent fraction at the bottom interface and the free surface. The *ex situ* GISAXS measurements performed on one deposited BST layer on SiO<sub>2</sub>/Si annealed at 600 °C show that the evaporation should last at least 30 min, i.e., 1800 s in order to remove the organic compounds from the film. For an annealing time of 2000 s, for example, using  $\eta_s = 0.8$  mPa.s,  $\ell_i \sim 25$  μm,  $x_{si} = 0.07$ , one gets  $\psi_d - \psi_u \sim 0.15\%$ . With one final annealing at high temperatures, the annealing time necessary to remove the organic constituents is very long, as the evaporation time is proportional to the square of the film thickness.

This model may also explain the difference in growth morphology according to the high temperature annealing types. Let us explain the observed granular growth observed for the 2 L annealing. The solution diffusion is initiated at the bottom of the additional deposited layer where the solvent fraction is larger, i.e., above the inorganic NPs, as shown in Fig. 11(a). For this reason, the diffusion flow brings the inorganic constituents laterally, shifted with respect to the particles in the previous layer. The final morphology obtained after the 2 L annealing at high temperatures is represented

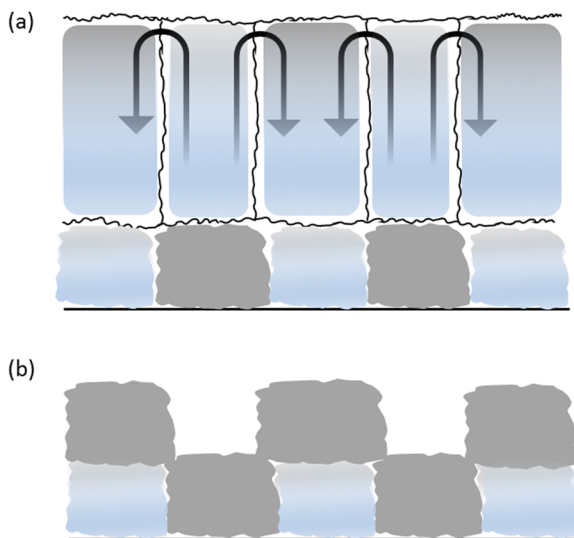


**FIG. 11.** Convection-driven morphology of an additional deposited layer for 2 L annealing (a) at the beginning of convection and evaporation for the additional layer and (b) at the end of this process and after annealing at high temperatures. The inorganic fraction (respectively, solvent) is represented by gray (respectively, blue) shading.

in Fig. 11(b). On the contrary, for a 1 L annealing at high temperatures, a columnar growth is observed. The solution diffusion is initiated where the solvent fraction is larger, i.e., above the pores, as shown in Fig. 12(a). For this reason, the diffusion flow brings inorganic constituents above the particles of the previous layer, resulting in the columnar growth. The final morphology obtained after the 1 L annealing at high temperatures is represented in Fig. 12(b). In short, the growth type is not fundamentally linked to a thickness criterion, but to the amount of organic constituents left. Whatever the high temperature annealing types are, the deposition of additional layers occurs with heterogeneous nucleation.

#### D. Electrical properties

The electrical properties of the 1 L and 2 L samples were investigated. The dielectric constant and the loss tangent were calculated using the following equations:

$$C = \frac{\epsilon_0 \epsilon_r A}{d}, \quad (15)$$

$$\tan \delta = \frac{1}{2\pi C_p R_p f}, \quad (16)$$

where  $\epsilon_r$  is the dielectric constant,  $\epsilon_0$  is the air permittivity ( $8.85 \times 10^{-12}$  F/m),  $A$  is the capacitor area ( $7.85 \times 10^{-7}$  m<sup>2</sup>),  $d$  is the thin film thickness (440 nm),  $C_p$  is the parallel capacitance (F),  $R_p$  is the parallel resistance ( $\Omega$ ), and  $f$  is the frequency (Hz).<sup>31</sup>

Figure 13 shows the different electrical properties of the 1 L and 2 L thin film capacitors. The capacitance degradation in Fig. 13(a) for the 2 L sample is due to the organic residues in the thin film structure in comparison to the 1 L sample, which presents good capacitive

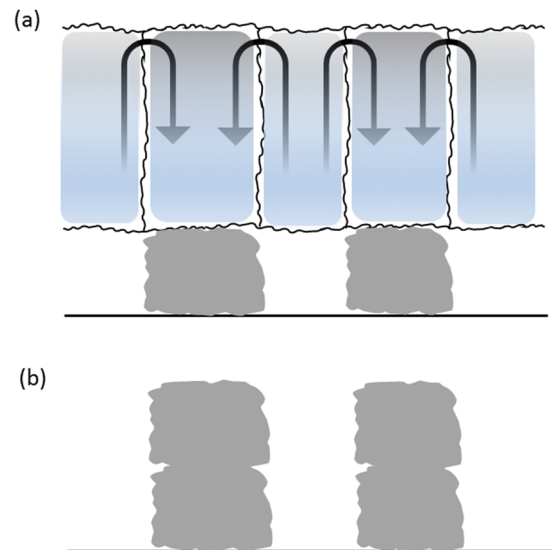


**FIG. 12.** Convection-driven morphology of an additional deposited layer for 1 L annealing (a) at the beginning of convection and evaporation for the additional layer and (b) at the end of this process and after annealing at high temperatures. The inorganic fraction (respectively, solvent) is represented by gray (respectively, blue) shading.

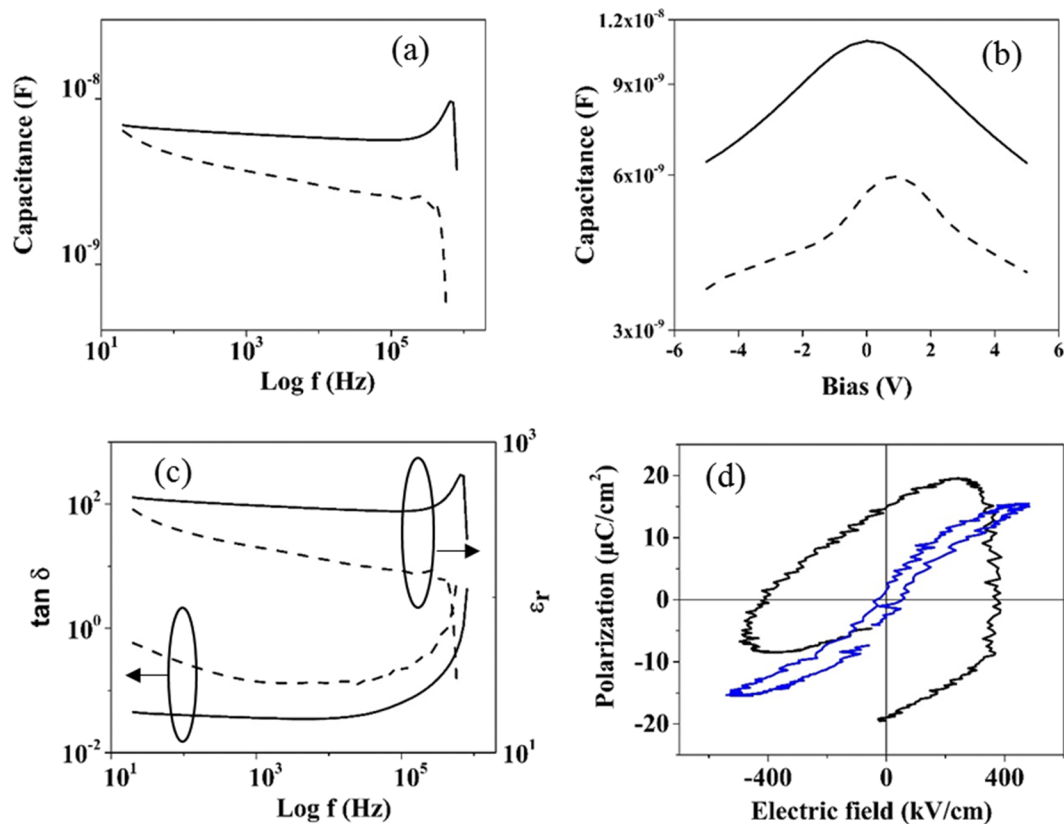


**FIG. 13.** (a) Capacitance vs frequency, (b) capacitance vs voltage at the frequency of 1 kHz, and (c) dissipation factor and dielectric constant vs frequency. Annealing of 1 L (solid line) and 2 L (dotted line). The abnormality at  $10^6$  Hz is due to the machine limitation (20 Hz–1 MHz). (d)  $P$ – $E$  field curve of 1 L (blue) and 2 L (black) at a frequency of 100 Hz.

behavior for a BST capacitor. Figure 13(b) shows the capacitance as a function of voltage measured at 1 kHz for both samples. The 1 L sample has higher capacitance values, higher dielectric constants, and a lower dissipation factor than 2 L, as shown in Fig. 13(c). For example, at 10 kHz, the 1 L sample has a dielectric constant of 371 and a dissipation factor of  $\sim 0.035$ , and the 2 L sample has a dielectric constant of 178 and a dissipation factor of  $\sim 0.133$ . Hence, the electrical properties of BST thin films are improved for 1 L annealing. Compared to the work of Adikary *et al.*,<sup>9</sup> the dielectric constant of the 1 L sample is divided by 2.2 and the dissipation factor is smaller by one order of magnitude. Finally, Fig. 13(d) displays the polarization–electric field measurements of the BST films at RT. The typical hysteresis loop of the 1 L sample indicates effective switching of the dipoles. The ferroelectric characteristics are remnant polarization of  $\sim 1.2 \mu\text{C}/\text{cm}^2$ , a saturation polarization of  $\sim 15 \mu\text{C}/\text{cm}^2$ , and a coercive field of  $\sim 54$  kV/cm. On the contrary, the 2 L sample has no ferroelectric hysteresis loop. Actually, the  $P$ – $E$  field curve may reveal polarization of space charge from organic constituents.<sup>32</sup> In the 2 L sample, organic constituents are left leading to a significant amount of ions. A high remnant polarization occurs due to the trapping of the ions on the electrode and a high field is required to extract them from the electrode, move them into the film, and decrease the

polarization. In short, the left organic constituents are responsible for the non-ferroelectric behavior of the 2 L sample.

#### IV. CONCLUSIONS

The morphology of sol–gel processed BST thin films was investigated as a function of thermal annealing. GISAXS allowed the study of nano-sized domains from the liquid film to the dry one as a function of the annealing temperature. During annealing at low temperatures, domains can be self-organized in the direction parallel to the surface. At higher temperatures, the inorganic-rich and organic-rich domains lead to nanocrystals and pores, respectively, after solvent evaporation. During cooling, the pore shape changes due to the thermal contraction of the substrate. In addition, films obtained with extremely thin layers and with 1 L annealing at high temperatures present columnar growth. A general flow model based on the physics of fluids gives a deep insight into sol–gel thin film elaboration at the nanometer-scale. For the first time, the columnar growth in sol–gel thin films is directly linked to the complete removal of organic constituents in the previous deposited layer. Finally, the ferroelectric hysteresis loop was obtained after the removal of organic constituents, achieved by depositing extremely thin layers and 1 L

annealing at high temperatures. Thus, our findings allow tailoring of sol-gel thin films at the nanoscale and development of cost-effective ferroelectric thin films on large surfaces.

## ACKNOWLEDGMENTS

We would like to thank N. Boudet, N. Blanc, and the technical staff of BM02 for assistance during the GISAXS experiment. We acknowledge the French CRG committee for provision of synchrotron radiation beamtime.

This research did not receive any specific grant from funding agencies in the public, commercial, or not-for-profit sectors.

The authors declare that they have no conflict of interest.

## DATA AVAILABILITY

The data that support the findings of this study are available from the corresponding author upon reasonable request.

## REFERENCES

- <sup>1</sup>P. Muralt, *J. Micromech. Microeng.* **10**, 136 (2000).
- <sup>2</sup>L. B. Kong, T. Li, H. H. Hng, F. Boey, T. Zhang, and S. Li, *Waste Energy Harvesting* (Springer-Verlag, Berlin Heidelberg, 2014).
- <sup>3</sup>A. K. Batra and M. D. Aggarwal, *Pyroelectric Materials: Infrared Detectors, Particle Accelerators, and Energy Harvesters* (SPIE Press, 2013).
- <sup>4</sup>K. Nadaud, C. Borderon, R. Gillard, E. Fourn, R. Renoud, and H. W. Gundel, *Thin Solid Films* **591**, 90 (2015).
- <sup>5</sup>Y.-C. Liou and C.-T. Wu, *Ceram. Int.* **34**, 517 (2008).
- <sup>6</sup>T. R. Taylor, P. J. Hansen, B. Acikel, N. Pervez, R. A. York, S. K. Streiffer, and J. S. Speck, *Appl. Phys. Lett.* **80**, 1978 (2002).
- <sup>7</sup>D. Levasseur, H. B. El-Shaarawi, S. Pacchini, A. Rousseau, S. Payan, G. Guegan, and M. Maglione, *J. Eur. Ceram. Soc.* **33**, 139 (2013).
- <sup>8</sup>M. E. Azim Araghi, N. Shaban, and M. Bahar, *Mater. Sci.-Pol.* **34**, 63 (2016).
- <sup>9</sup>S. U. Adikary and H. L. W. Chan, *Thin Solid Films* **424**, 70 (2003).
- <sup>10</sup>S. Budiawanti, B. Soegijono, and I. Mudzakir, *J. Phys.: Conf. Ser.* **985**, 012034 (2016).
- <sup>11</sup>A. Pierre, *Introduction to Sol-Gel Processing* (Springer, 1998).
- <sup>12</sup>M. C. Gust, L. A. Momoda, N. D. Evans, and M. L. Mecartney, *J. Am. Ceram. Soc.* **84**, 1087 (2001).
- <sup>13</sup>S. B. Singh, H. B. Sharma, H. N. K. Sarma, and S. Phanjoubam, *Physica B* **403**, 2678 (2008).
- <sup>14</sup>L. Zhang, W.-L. Zhong, C.-L. Wang, P.-L. Zhang, and Y.-G. Wang, *J. Phys. D: Appl. Phys.* **32**, 546 (1999).
- <sup>15</sup>R. W. Schwartz, T. Schneller, and R. Waser, *C. R. Chimie* **7**, 433 (2004).
- <sup>16</sup>C. Revenant, M. Benwadih, and M. Maret, *Chem. Commun.* **51**, 1218 (2015).
- <sup>17</sup>L. L. Yang, D. T. Ge, X. D. He, F. He, Y. B. Li, and S. Zhang, *Thin Solid Films* **517**, 5151 (2009).
- <sup>18</sup>C. Revenant and M. Benwadih, *Thin Solid Films* **616**, 643 (2016).
- <sup>19</sup>P. G. de Gennes, *Eur. Phys. J. E* **6**, 421 (2001).
- <sup>20</sup>D. Sette, V. Kovacova, and E. Defay, *Thin Solid Films* **589**, 111 (2015).
- <sup>21</sup>G. A. Chahine, N. Blanc, S. Arnaud, F. De Geuser, R. Guinebrière, and N. Boudet, *Metals* **9**, 352 (2019).
- <sup>22</sup>D. Babonneau, *J. Appl. Cryst.* **43**, 929 (2010).
- <sup>23</sup>W. Ma, *Appl. Phys. A* **96**, 915 (2009).
- <sup>24</sup>Y.-W. Sheu and C.-H. Tu, *J. Chem. Eng. Data* **51**, 1634 (2006).
- <sup>25</sup>P. G. de Gennes, *Macromolecules* **14**, 1637 (1981).
- <sup>26</sup>C. Revenant, F. Leroy, R. Lazzari, G. Renaud, and C. R. Henry, *Phys. Rev. B* **69**, 035411 (2004).
- <sup>27</sup>D. W. Schaefer, J. E. Martin, P. Wiltzius, and D. S. Cannell, *Phys. Rev. Lett.* **52**, 2371 (1984).
- <sup>28</sup>B. L. Henke, E. M. Gullikson, and J. C. Davis, *At. Data Nucl. Data Tables* **54**, 181 (1993).
- <sup>29</sup>Z.-G. Ban and S. P. Alpay, *J. Appl. Phys.* **91**, 9288 (2002).
- <sup>30</sup>L. Zhang, M. Ichiki, and R. Maeda, *J. Eur. Ceram. Soc.* **24**, 1673 (2004).
- <sup>31</sup>M. A. Salam and Q. M. Rahman, *Fundamentals of Electrical Circuit Analysis* (Springer, Singapore, 2018).
- <sup>32</sup>H. Kliem and B. Martin, *J. Phys.: Condens. Matter* **20**, 321001 (2008).